AERIAL CLOSE-RANGE PHOTOGRAMMETRY TO QUANTIFY DEFORMATIONS OF THE PILE RETAINING WALLS

Abstract

Today, as structures with life expectancy of more than 100 years are being constructed, it is vital to gain knowledge about the gradual decline in material properties. Accordingly, to ensure the longevity and safety of these structures, monitoring has been incorporated as a fundamental part of their service life. To monitor structural deformation, various methods have been developed, with the most common being the survey of certain points of a structure during and after construction using a total station. New techniques are now being developed, and one of the most promising ones is photogrammetry because it provides a simple method to monitor a structure using Unmanned Air Vehicles (UAVs). This paper is aimed at sharing the strategic steps followed in monitoring the deflection of a simple secant pile retaining wall during excavation and construction of a basement. The monitoring is performed using a commercial UAV in combination with point cloud formation, georeferencing, and comparison software (cloud compare, I-Site Studio, 3DReshaper etc.). The monitoring results show very good agreement with the traditional inclinometer deflection measurements and numerical analysis, thereby demonstrating the feasibility of the proposed method. The authors believe that in the future, photogrammetry using UAVs can become the standard method for geotechnical monitoring because its speed, lower cost and ease of use, when compared to conventional methods, a non-destructive method, and is easy to learn and use.

Keywords: Photogrammetry, Monitoring, Unmanned Air Vehicle (UAVs), Image processing, Structural deformation.

1. Introduction

Structures around the world undergo deformation because of weather conditions, groundwater, seawater, earthquakes, and many other natural factors. Structures requiring deep excavations, terraces on slopes, retaining walls, and embankment slopes along highways and roadways are geotechnical assets, which are a critical part of national infrastructure systems. These geotechnical assets can fail during construction or along their service life, because of various problems including the lack of proper design or maintenance, deterioration of materials, and use of unregulated backfill or poor drainage systems [1–4]. Specifically, in retaining structures, failure mechanisms are triggered by deep-seated movement, overturning motion, bearing capacity, or sliding translation [2, 5]. Therefore, monitoring of these structures is necessary to secure their construction and maintain safety. In addition to structural monitoring during the life cycle of assets, it is important to monitor the deformations during the construction phase. Monitoring the construction phase is an essential process for geotechnical assets because the soils can be extremely heterogeneous; particularly on large construction sites, where design depend on parameters determined using spot site investigations (standard penetration test, cone penetration test, pressuremeter test, etc.), the appearance of unforeseen soil conditions can lead to unexpected responses from the structure. Therefore, structural monitoring, back analysis, and design modification are extremely important steps during the construction of geotechnical structures. Various monitoring techniques have been developed to monitor deformations. These techniques can be categorized as conventional measuring methods (precise leveling or total station surveying), positioning system methods (Global Positioning System (GPS) measurement), satellite radar system methods (Interferometric synthetic aperture radar (InSAR) observation), photogrammetry (satellite, aerial, or earthbound imaging), some traditional geotechnical methods using inclinometers and strain meters and, more recent, fibre optics either Brillouin or Bragg techniques.

Table 1 summarises the advantages and disadvantages of certain important above-mentioned monitoring techniques used in the field. Geotechnical monitoring equipment's such as fiber optic strain sensors [42] and inclinometers [43] are widely used in pile deformation monitoring. Even though, using fibre optic Brillouin strain sensors you could obtain three-dimensional deformed shape with high accuracy, they are known to use very expensive analysers. Furthermore, both devices are offering local solutions as they should be installed in/on to the structure and physical contact with the structure is required to obtain the measurements. Contact devices such as conventional surveying equipment [31, 37] and global navigation satellite systems (GNSSs) [13-16, 36] have been used to monitor structural deformation or slope movement, but these devices can be expensive or time consuming, can be limited by physical or traffic accessibility problems, or can have low accuracy in determining real-time movements. The use of Terrestrial Laser Scanners (TLS) [8, 39, 40] has also been incorporated in monitoring; however, it is a costly method but it has been decreasing in price. Interferometric synthetic aperture radar (InSAR) [32-35, 38] observation has also been utilized in the field of displacement measurement however, it experiences some drawbacks in that it is a time-consuming method with limited vertical displacement measurement and a single look direction whose accuracy can be affected by different weather conditions.

Therefore, more recently, to reduce the cost and ease the monitoring process, photogrammetry [6, 7, 17, 44] has been utilized. Renee et al. [23] used 3D photogrammetry to assess the failure modes of a sample retaining wall model. This new solution was proposed as a cost-effective, fast, and safe asset management system, which could be an alternative to existing retaining wall monitoring techniques. PhotoScan software was used to produce dense points, compare the locations of common points representing the surfaces for different scenarios, and determine the surface displacements. Additionally, control points that did not move between epochs were used to co-register the point clouds in a coordinate system common to the different epochs. Finally, control points on the moving panels were compared between epochs, and the comparison was also carried out using conventional surveying techniques. The results of this study indicated that the accuracy of displacement between the two methods was within 1–3 cm. Photogrammetry provides speed and cost effectiveness to the monitoring process; however, the accuracy of photogrammetry depends on the distance from which the photograph is taken as well as the type of camera. Furthermore, it is difficult to use photogrammetry in areas with restricted access or in large project sites.

To overcome the abovementioned disadvantages, photogrammetry with the aid of Unmanned Air Vehicles (UAVs, commonly known as drones) [18-20, 41] have been introduced and used extensively in the field of civil engineering. In a study, Brown [24] used the locations and elevations of surveyed auger holes and the ground surface as control points and aligned two point clouds, which were generated from autonomous flight paths of Unmanned Air Vehicle (UAVs) , by picking common points in CloudCompare software. To interpolate a surface from the lowest point, Brown [24] manually cleaned the point cloud in CloudCompare by removing trees and other “noise” that did not represent the ground surface. More recently, Turner et al. [20] monitored possible unfavourable discontinuities in underground excavations using the UAV imagery. Upon successfully generating and georeferencing the point cloud model, they used CloudCompare to align the unregistered RGB, thermal, and multispectral models with the registered LIDAR data from the slopes.

In this study, the authors utilized the close-range photogrammetry technique along with the UAV to enable reaching of difficult-to-access areas faster and more economically; the UAV obtained photographs, which were converted to point cloud data, and the deformations occurring on the geotechnical structure were further analysed. Furthermore, the geometry obtained via the point clouds was provided to numerical analysis software to analyse the expected deformations. Finally, the expected deformations calculated via the numerical software and measured with inclinometer were compared against the proposed monitoring data obtained on site.

2. Method

The images collected by the UAV are processed in the following stages: 3D point cloud formation, georeferencing, and point cloud comparison. In photogrammetry, the formation of a 3D point cloud is a process that involves various steps. To accomplish these steps, various software packages can be used. Harwin and Lucieer [21] mentioned commonly used software such as PhotoScan (Agisoft) and PhotoModeler as well as open-source platforms such as Photosynth and Bundler [22]. In addition, software such as CloudCompare, I-Site Studio, and 3DReshaper can be used for georeferencing and the comparison of point clouds from different epochs by aligning them using existing reference points in different 3D models [25-27].

2.1.1. Image Collection

Figure 1 shows the steps used for conducting the photogrammetry study on the site discussed in the paper. Flow chart is also aligned with the flow of this study from this point onwards. First, a site walkover survey was conducted, after which a desk study, recording the topography of the study area as well as planning the location of the targets, was undertaken. It should be noted that the desk study was conducted after the walkover survey because input from the site conditions was required for planning the survey and target location. Following the desk study, 10 printed retroreflective targets were placed on site. According to the conditions seen on site, the targets were printed on an A4 sized paper and later laminated to provide more resistance to weather and dust. These steps facilitated easy alignment from one epoch to another. The location as well as the number of targets placed differed from site to site. The location of the targets was heavily dependent on the topography of the study area. As seen on Figure 2 retroreflective targets were also used as ground control points and coordinates of the points have been recorded with an aid of Pentax Series G6 GNSS device (Table 2).This coordinates of ground control points (known points) were recorded in order to improve the accuracy of the point cloud or the Digital Elevation Model (DEM) generated using the UAVs.

A UAV (DJI PHANTOM 3 Pro) equipped with a 12-megapixel camera (Sony EXMOR) (see Table 3 for camera specifications) was used to manually capture around 120 pictures from the site on every epoch. The pictures were taken following a simple rule: every picture overlapped, by at least 70%, every surrounding picture. Prior to image collection, the device quality, including the battery life and flashcard memory space, were checked. One battery with a battery life of 25 min was sufficient for monitoring a 200-m-long, 8-m-high retaining wall.

2.1.2. Image Processing

Image processing and alignment were carried out using PhotoScan, which was chosen because it provides an affordable solution for multiview 3D construction. James and Robson [28] stated that the structure-from-motion approach requires multiple pictures of an object from more than one camera angle and an overlapping ratio of at least 70% for accurate 3D reconstruction. At the site, measurements were taken to ensure that the above criteria were met and about 120 photographs were taken at each epoch. Captured images were in .jpg format and their sizes were 4000×3000 pixels. Images were stored on a video speed class (V_{90}) micro SD card to enable fast recording. Images were directly imported from the micro SD card to the computer with a DJI link cable. Prior to uploading the photographs to the software, poor-quality, dislocated and blur images were deleted as they would have reduced the quality of the 3D point cloud construction. Within the software environment, camera calibration that would provide a correct point cloud is not necessary because the software estimates the camera calibration parameters automatically using Brown's model [45] for lens distortion; a process known as bundle adjustment. Camera calibration is advantageous in that it enables the user to remove pictures that do not offer good precision. Therefore, manual calibration is not needed if standard optical lenses and a highly redundant image network is used.

After loading the taken photographs in PhotoScan, the images are aligned. This process iteratively refines the internal as well as external camera orientations and locations using the least-squares solution. This process takes about 10 minutes to complete. The software then builds a sparse point cloud model and calculates the depth information based on the estimated camera positions. A single dense point cloud can be obtained using the "Build dense point cloud" command. In the case study outlined below, in generating the dense cloud about 10 million points were obtained and the process took about 160 minutes. Furthermore, the software allows the user to set the quality and depth for the point cloud generation. Settings for achieving higher quality can also be obtained; however, this will require a longer processing time. The dense point cloud obtained was then cleaned for about 10 minutes by cutting out points that will interfere with analysis. It is worth to mention that the above mentioned durations for processing depends on the computer configuration and in this current case an i7-7700HQ CPU at 2.8GHz with 16GB of RAM and a K5000 graphics card and a 1TB SSD hard drive computer was used.

2.1.3. Data Processing

After data from two different epochs were obtained, the generated point clouds were exported to the CloudCompare software in the LAZ (Lidar Data file) format. CloudCompare is an open-source software that allows operations and comparisons to be performed on 3D point clouds from different epochs. Prior to carrying out any comparison, CloudCompare's Iterative Closed Point Processing algorithm is used to align the two point clouds. Close overlap between the targets is necessary for the best alignment of the point clouds. Girardeau-Montaut [29] reported that noise and points outside the area of interest should be removed before performing the alignment and registration to prevent the degradation of the registered point clouds.

Change detection, as described by Singh [30], refers to the process of identifying the differences in an object by observing it at two epochs. While carrying out change detection, the areas in the point cloud where changes occurred were analyzed more closely.

In CloudCompare, analysis of change detected areas can be carried out primarily in two different forms—cloud-to-cloud and cloud-to-mesh—both of which are used in this study. In these two methods, first the point cloud is sectioned and these sections are then closely analysed, as shown in Figure 3a. In the cloud-to-cloud comparison, the software calculates the distance between a point on the first cloud and a group of points on the second cloud. The distance displayed is the shortest distance calculated (Figure 3b). In the cloud-to-mesh comparison, a series of planes are fitted to the point cloud and the distance perpendicular to the nearest plane is measured (Figure 3c). The distance from a point to a plane is measured (X1, X2, X3…Xn), as shown in Figure 3c. CloudCompare is then used to develop a Gaussian distribution graph that displays the number of points versus the distance measured between epochs (see the section on the case studies for the graph).

In this study, a new method of analysis called the strip method is also adopted. This method is similar to the cloud-to-cloud comparison, with the only difference being that the point cloud is cut into a longitudinal thin strip (Figure 3a and 3d). As a benefit in the current practice, the strip method allows the deflection along the length of the pile wall to be seen. After obtaining the deflection data from the CloudCompare, the data is exported to Microsoft Excel, where graphs are drawn; these graphs allow the user to better visualize the amount of deflection observed. Furthermore, the angle of deflection of the pile can similarly be estimated through geometric relations. Considering that the wall length remains the same and no axial load is applied on the pile cap, than there is no axial deformation on the wall; the angle Δ at the base of the wall is twice the angle α, as shown in Figure 3d.

3. Case Study

3.1. Pile Retaining Wall Monitoring during Deep Excavation

To investigate the use of the proposed method, a cantilever pile retaining wall of the basement of an apartment block was monitored. The authors of this paper were responsible for performing site investigations to obtain the relative soil parameters for the design and monitoring of the retaining wall deformations during the construction phase. The studied apartment block is located in the district of Kyrenia, Northern Cyprus. The proposed structure has seven stories with two basement levels and is constructed using reinforced concrete. Therefore, to construct the basement, an excavation depth of 7.5 m is proposed, and the excavation was performed in four stages.

3.1.1. Study Area

Figure 4 shows the layout of the studied site. At a 5-m distance from the east face of the excavation site, there is a single-story reinforced-concrete structure (A). On the west side, there is a two-lane road (B), which carries heavy traffic to the commercial port, and on the north side, there is a single-lane town road (C), which carries light traffic. On the south side of the excavation site, there is a swimming pool (D) at a distance of 2 m and a two-story reinforced-concrete structure (E) at a distance of 9 m.

To obtain the geotechnical parameters for design purposes, five standard penetration tests (one at each of the four corners and one at the centre of the site) and laboratory tests were performed. The encountered soil profiles consisted of sandy clay up to 2 m, silty clay down to 5.5 m, stiff clay down to 11 m, and marl down to 20 m. At this level, the investigation was stopped because the marl was assumed to be the bedrock, extending to a depth of 2 km. The water table on site was found to be at 3 m from the ground level. The decision to use a secant pile wall was attributed to the unsafe conditions along the slope on the western side, where the road with the heavy traffic existed. To construct the proposed basement, a cantilever retaining wall (Figure 5) was proposed. To evaluate the lateral earth pressures acting on the wall, an idealized soil profile was formed by adopting a Mohr–Coulomb soil model and using the effective soil parameters obtained from the site investigations and laboratory testing results. The parameters used for each soil layer are listed in Table 4.

Finite element modelling software (Plaxis 2D v.8.6) was used to perform two-dimensional analysis on the proposed pile retaining wall under the current loading conditions. A stage-wise construction method was used in the analysis. In the first stage, the initial (geostatic) conditions of the ground were considered; here, just the piles were constructed but no excavation was performed. This stage was followed by four stages, representing the soil excavation and the epochs of monitoring. Therefore, the numerical calculations consisted of a geostatic condition and four consecutive stages of excavation, after which the final condition was reached (Figure 6). Following the analysis, Figure 7a shows the deformations occurred along the analysed area with the deformations occurring on the pile retaining wall. According to the results, the maximum horizontal displacement of 32 mm occurred at the top of the wall. The variations in the horizontal deformations along the pile surface are shown in Figure 7b, which indicates that the deformation reduced as the excavation level progressed downward.

Furthermore, an inclinometer was installed at the central bored pile and displacements were recorded at two different dates, starting from the beginning of pile wall construction. It can be seen on Figure 8 that the maximum deformation is at the pile capping beam, reducing with the increase in depth. The maximum displacement measured in two different epochs are at the pile capping beam and correspond to 15mm on 06.09.2017 and 52mm on 17.09.2017. The location of the installed inclinometer is indicated as location B in Figure 9.

3.1.2. Results

A comparison of the generated point clouds consisted in the computation of the distance between two point clouds from four different epochs. The chosen segments are shown in Figure 9. These segments are labelled as A, B, and C in the horizontal direction, and their relative depths from the top of the capping beam are 0, -2, and -4 m. Based on the visual horizontal deformations, segments were further chosen depending on the performed numerical analysis. Two segments were chosen close to the corners where the expected deformations were much lower because of the corner effect of the retaining structure, and one segment was chosen in the middle, where high deformations were expected.

Figure 10 shows the Gaussian distribution of the cloud-to-cloud distances with respect to the depths of 0, -2, and -4 m along the selected pile surface at location C. As expected, the deformation at the top of the pile was 16.88 mm and reduced to 6.94 mm at the depth of -4 m. It was not possible to compare the displacement of the wall at the bottom of the excavation site because the point clouds were generated at different excavation levels.

Figure 11 shows the comparison of the cloud-to-cloud distance at location A for the intervals between epochs 1 and 2, 1 and 3, and 1 and 4. As time passed, the deformation of the wall increased from 21 mm in epoch 2 to 63 mm at the final epoch. Figure 12 shows the comparison of the cloud-to-mesh approach used to analyse the deformations at the same location A. The results were in good agreement with those of the cloud-to-cloud comparison at the same location.

Table 5 lists the maximum displacements at the pile capping beam along the selected locations at different epochs for both the cloud-to-cloud and cloud-to-mesh methods, showing that both methods are consistent. As time progressed, the deformations at the top of the beam at all the locations increased. Additionally, location A showed the highest deformation among the all locations. Location C showed the least deformation because it was closest to the corner and was influenced by the corner effect.

The comparison of the two developed methods indicated that the cloud-to-cloud method gave results that were more logical. As an extension of this method, a cloud-to-cloud comparison method along a strip was developed. Figure 13 shows the comparison of strips from different epochs at location B. To observe the deformations in a more pronounced manner, Figure 14 was plotted. This figure focuses on the pile cap section because it was found to show the highest deformations according to the inclinometer measurements and numerical analysis.

The progress of the deformations measured via strip, cloud to cloud and inclinometer measurements at the pile capping beam, at different epochs and at location B are shown in Table 6. Displacements measured via each method were plotted against time in days on Figure 15. A comparison of the results in Figure 15 and those in Table 6 indicate that the measurements are consistent, showing similar results. The curves for each method seem to adjust in a polynomial curve. Therefore, it is clear that the results of aerial close-range photogrammetry are in good agreement with the inclinometer measurements.

4. Conclusions and Recommendations

In this study, two different methods of deformation monitoring via aerial photogrammetry have been adopted: cloud-to-cloud and cloud-to-mesh methods. A novel strip method has also been proposed as an extension of the cloud-to-cloud method. Among the three adopted methods, the strip method is found to reveal the full deformation profile of the pile and was found to be the easiest and quickest to apply. Additionally, by reducing the number of points relative to the other two methods and using widely known software such as Microsoft Excel, the strip method can eliminate the need for complex analysis on CloudCompare and the requirement of large computational power, often required by these softwares. Furthermore, the results of the photogrammetric study are in alignment with those of the inclinometer measurements during the construction of the wall. For all the numerical, inclinometer and proposed methods, the expected deformations are the greatest at the top of the pile cap and reduce as the excavation progresses down to the bottom of the site.

Compared to other available photogrammetry techniques, the proposed method enables close-range photogrammetry to be carried out using a UAV. Therefore, the difficult-to-access areas of geotechnical structures (deep excavations, slopes with stability problems, and retaining structures) can be monitored with high accuracy.

Furthermore, it is considerably quicker and easier to obtain data on a geotechnical field using the proposed method than using other available techniques. With the advancements in drone technology, route planning that allows inspection scheduling in advance can be performed; in this case, drones can autonomously fly off and collect data at predefined locations and return to their docking stations. Moreover, the proposed technique records considerable geometric data in a brief period, by procuring pictures using easy-to-use cameras. This permits users to return to the visual records and conduct extra investigations at a later stage.

The disadvantage of the adopted methods is that the displacement of the wall at the bottom of the excavation site cannot be compared because the point clouds are generated as the different excavation levels progress. Furthermore, it is recommended that a similar study be conducted by comparing the findings of the proposed methods with the results obtained using known deformation monitoring tools such as GNSSs, inclinometers, and laser scanners so that the accuracy of the proposed methods can be examined.

References

[1] Anderson SA, Rivers BS (2013) Capturing the impacts of geotechnical features on transportation system performance. In: Meehan C, Pradel D, Pando MA, Labuz JF (eds) Proceedings of geo-congress, San Diego, CA, USA, March 3–7, 2013. American Society of Civil Engineers, Virginia, USA, pp 1633–1642. https://doi.org/10.1061/9780784412787.164

[2] Budhu M (2000) Soil mechanics & foundations. John Wiley & Sons, Inc., Hoboken, NJ, USA.

[3] Duncan C (1992) Soils and foundations for architects and engineers. Springer Science and Business Media, Norwell, MA, USA.

[4] Mohammad T (2005) Failure of a ten-story reinforced concrete building tied to retaining wall: evaluation, causes, and lessons learned. In: Proceedings of structures congress, New York, USA, April 20–24, 2005. American Society of Civil Engineers, Virginia, USA, https://doi.org/10.1061/40753(171)239

[5] Bernhardt KLS, Loehr JE, Huaco D (2003) Asset management framework for geotechnical infrastructure. J Infrastruct Syst 9(3):107–116. https://doi.org/10.1061/(ASCE)1076-0342(2003)9:3(107)

[6] Han J, Hong K, Kim S (2012) Application of a photogrammetric system for monitoring civil engineering structures. In: Da Silva DC (ed) Special applications of photogrammetry IntechOpen, Rijeka, Croatia, pp 73–96. https://doi.org/10.5772/34906

[7] Scaioni, M., Barazzetti, L., Giussani, A. et al. Photogrammetric techniques for monitoring tunnel deformation. Earth Sci Inform 7, 83–95 (2014). https://doi.org/10.1007/s12145-014-0152-8

[8] Wang G, Philips D, Joyce J, Rivera F (2011) The integration of TLS and continuous GPS to study landslide deformation: a case study in Puerto Rico. J Geod Sci 1(1):25–34. https://doi.org/10.2478/v10156-010-0004-5

[9] Escobar-Wolf R, Oommen T, Brooks C, Dobson R, Ahlborn T (2017) Unmanned aerial vehicle (UAV)-based assessment of concrete bridge deck delamination using thermal and visible camera sensors: a preliminary analysis. Res Nondestr Eval 29(4):183–198. https://doi.org/10.1080/09349847.2017.1304597

[10] Jauregui DV, White KR, Woodward CB, Leitch KR (2003) Noncontact photogrammetric measurements of vertical bridge deflection. J Bridge Eng 8(4):212. https://doi.org/10.1061/(ASCE)1084-0702(2003)8:4(212)

[11] Jiang R, Jauregui DV, White KR (2008) Close-range photogrammetry applications in bridge measurement: literature review. Measurement 41(8):823–834. https://doi.org/10.1016/j.measurement.2007.12.005

[12] Vaghefi K, Oats R, Harris D, Ahlborn T, Brooks C, Endsley K, Roussi C, Shuchman R, Burns J, Dobson R (2012) Evaluation of commercially available remote sensors for highway bridge condition assessment. J Bridge Eng 17(6):886–895. https://doi.org/10.1061/(ASCE)BE.1943-5592.0000303

[13] Erol S, Erol B, Ayan T (2004) A general review of the deformation monitoring techniques and a case study: analyzing deformations using GPS/leveling. In: Proceedings of XXth ISPRS congress, Istanbul, Turkey, July 12–23, 2004. International Society for Photogrammetry and Remote Sensing, Hannover, Germany, pp 12–23.

[14] Xu K, Gan W, Wu J (2019) Pre-seismic deformation detected from regional GNSS observation network: a case study of the 2013 Lushan, eastern Tibetan Plateau (China), Ms 7.0 earthquake. J Asian Earth Sci 180:103859. https://doi.org/10.1016/j.jseaes.2019.05.004

[15] Luo L, Ma W, Zhang Z, Zhuang Y, Zhang Y, Yang J, Mu Y (2017) Freeze/thaw-induced deformation monitoring and assessment of the slope in permafrost based on terrestrial laser scanner and GNSS. Remote Sens 9(3):198. https://doi.org/10.3390/rs9030198

[16] Yang Y, Zheng Y, Yu W, Chen W, Weng D (2019) Deformation monitoring using GNSS-R technology. Adv Space Res 63(10):3303–3314. https://doi.org/10.1016/j.asr.2019.01.033

[17] Masoodi A, Noorzad A, Majdzadeh Tabatabai MR, Samadi, A (2018) Application of short-range photogrammetry for monitoring seepage erosion of riverbank by laboratory experiments. J Hydrol 558:380–391. https://doi.org/10.1016/j.jhydrol.2018.01.051

[18] Yutaka W, Yoshihisa K (2016) UAV photogrammetry for monitoring changes in river topography and vegetation. Procedia Eng 154:317–325. https://doi.org/10.1016/j.proeng.2016.07.482

[19] Congress SSC, Puppala AJ (2019) Evaluation of UAV–CRP data for monitoring transportation infrastructure constructed over expansive soils. Indian Geotech J. https://doi.org/10.1007/s40098-019-00384-4

[20] Turner RM, MacLaughlin MM, Iverson SR (2020) Identifying and mapping potentially adverse discontinuities in underground excavations using thermal and multispectral UAV imagery. Eng Geol 266:105470. https://doi.org/10.1016/j.enggeo.2019.105470

[21] Harwin S, Lucieer, A (2012) Assessing the accuracy of georeferenced point clouds produced via multi-view stereopsis from unmanned aerial vehicle (UAV) imagery. Remote Sens 4(6):1573–1599. https://doi.org/10.3390/rs4061573.

[22] Snavely N, Simon I, Goesele M, Szeliski R, Seitz SM (2010) Scene reconstruction and visualization from community photo collections. Proc IEEE 98(8):1370–1390. https://doi.org/10.1109/JPROC.2010.2049330

[23] Renee O, Escobar-Wolf R, Oommen T (2017) A novel application of photogrammetry for retaining wall assessment. Infrastructures 2(3):10. https://doi.org/10.3390/infrastructures2030010

[24] Brown MKH (2016) 3D terrain and geological modelling for the design of a cut slope in Wellington. In: Proceedings of the 11th young geotechnical professionals conference, Queenstown, New Zealand, October 25–28, 2016. New Zealand Geotechnical Society, Wellington, New Zealand, pp 319–324.

[25] Vazaios I, Vlachopoulos N, Diederichs MS (2017) Integration of lidar-based structural input and discrete fracture network generation for underground applications. Geotech Geol Eng 35(5):2227–2251. https://doi.org/10.1007/s10706-017-0240-x

[26] Lato MJ, Vöge M (2012) Automated mapping of rock discontinuities in 3D lidar and photogrammetry models. Int J Rock Mech Min Sci 54:150–158. https://doi.org/10.1016/j.ijrmms.2012.06.003

[27] Dewez T, Girardeau-Montaut D, Allanic C, Rohmer J (2016) Facets: a Cloudcompare plugin to extract geological planes from unstructured 3D point clouds. Int Arch Photogramm Remote Sens Spatial Inf Sci XLI-B5:799–804. https://doi.org/10.5194/isprs-archives-XLI-B5-799-2016

[28] James MR, Robson S (2012) Straightforward reconstruction of 3D surfaces and topography with a camera: accuracy and geoscience application. J Geophys Res 117(F3):F03017, https://doi.org/10.1029/2011JF002289

[29] Girardeau-Montaut D (2011) CloudCompare: cloud to cloud compare workflow. http://www.danielgm.net/cc/forum/viewtopic.php?f=9&t=105. Accessed 17 March 2020

[30] Singh A (2010) Digital change detection techniques using remotely sensed data. Int J Remote Sens 10(6):989–1003. https://doi.org/10.1080/01431168908903939

[31] Kaloop M, Beshr A, Elshiekh M (2008) Using Total Station for monitoring the deformation of high strength concrete beams. 10.13140/2.1.1574.4006.

[32] Massonnet D, Rossi M, Carmona C, Adragna F, Peltzer G, Feigl K, Rabaute T (1993) The displacement field of the Landers earthquake mapped by radar interferometry. Nature, 364 (6433), 138.

[33] Rosen PA, Hensley S, Joughin IR, Li FK, Madsen SN, Rodriguez E, Goldstein RM (2000). Synthetic aperture radar interferometry. Proceedings of the IEEE, 88(3), 333–382.

[34] Yan Y, Doin M-P, Lopez-Quiroz P, Tupin F, Fruneau B, Pinel V, Trouvé E (2012) Mexico City subsidence measured by inSAR time series: Joint analysis using PS and SBAS approaches. IEEE Journal of Selected Topics in Applied Earth Observations and Remote Sensing, 5(4), 1312–1326.

[35] Sefa Y (2020) Validating InSAR-SBAS results by means of different GNSS analysis techniques in medium- and high-grade deformation areas. Environmental Monitoring and Assessment. 192. 10.1007/s10661-019-8009-8.

[36] Gu G, Wang W (2013) Advantages of GNSS in Monitoring Crustal Deformation for Detection of Precursors to Strong Earthquakes. Positioning, 4, 11-19. doi:10.4236/pos.2013.41003.

[37] Lienhart W (2017). Geotechnical monitoring using total stations and laser scanners: critical aspects and solutions. J Civil Struct Health Monit 7, 315–324. https://doi.org/10.1007/s13349-017-0228-5

[38] Thakur PK, Garg PK, Aggarwal SP (2013) Snow Cover Area Mapping Using Synthetic Aperture Radar in Manali Watershed of Beas River in the Northwest Himalayas. J Indian Soc Remote Sens 41, 933–945. https://doi.org/10.1007/s12524-012-0236-1

[39] Xu X, Bureick J, Yang H, Neumann I (2018) TLS-based composite structure deformation analysis validated with laser tracker, Composite Structures, Volume 202,Pages 60-65,ISSN 0263-8223.https://doi.org/10.1016/j.compstruct.2017.10.015.

[40] Gui H, Jun Y (2013) Deformation Monitoring for Subway Tunnels Based on TLS. Advanced Materials Research. 864-867. 2744-2749. 10.4028/www.scientific.net/AMR.864-867.2744.

[41] Stalin LJ, Gnanaprakasam RCP, (2020) Application of Unmanned Aerial Vehicle for Mapping and Modeling of Indian Mines. J Indian Soc Remote Sens 48, 841–852. https://doi.org/10.1007/s12524-020-01118-3

[42] Mohamad H, Soga K, Pellew A, Bennett PJ (2011) Performance monitoring of a secant-piled wall using distributed fiber optic strain sensing. Journal of Geotechnical and Geoenvironmental Engineering, 137(12), 1236-1243.

[43] Xu DS, Yin JH, Liu HB (2018) A new measurement approach for deflection monitoring of large-scale bored piles using distributed fiber sensing technology. Measurement, 117, 444-454.

[44] Valença J, Júlio ENBS, Araújo HJ (2012) Applications of photogrammetry to structural assessment. Exp Tech 36, 71–81. https://doi.org/10.1111/j.1747-1567.2011.00731.

[45] Brown DC (1966) Decentering distortion of lenses. Photogrammetric Engineering. 32 (3): 444–462.

Figure Captions:

Figure. 1. Flowchart representing the steps followed in aerial close-range photogrammetry study.

Figure. 2. Case study area aerial photographs and ground control points.

Figure. 3. Representation of (a) Pile arrangement cross section with mesh and strip sectioning (b) Cloud to cloud (c) Cloud to mesh and (d) Strip.

Figure. 4. Layout of the case study area.

Figure. 5. Proposed cantilever retaining wall.

Figure. 6. Numerical analysis showing stages of excavation, monitoring and analysis.

Figure. 7. Numerical analysis results (a) deformations along analyzed area and (b) variations of horizontal deformation along pile surface.

Figure. 8. Sketch of constructed cantilever retaining wall with inclinometer monitoring results.

Figure. 9. Point Cloud of the excavation area with the location of the sections used for comparison.

Figure. 10. Gauss distribution of Cloud to Cloud distance comparison at Location C at (a) 0m, (b) -2m, (c) -4m depth from reference point.

Figure. 11. Gauss distribution of Cloud to Cloud distance comparison at Location A (a) Epoch 1-2, (b) Epoch 1-3, (c) Epoch 1-4.

Figure. 12. Gauss distribution of Cloud to Mesh distance comparison at location A (a) Epoch 1-2, (b) Epoch 1-3, (c) Epoch 1-4.

Figure. 13. Comparison of epochs at location B with strip method.

Figure. 14. Deflections of the pile at location B from height 46.6m above sea level to 47.8m above sea level.

Figure. 15. Displacement of the pile capping beam at different epochs via Strip, Cloud to Cloud and Inclinometer measurements at location B.

Table Captions:

Table. 1. Comparison of different deformation monitoring techniques.

Table. 2. Control Point Coordinates taken by GNSS device.

Table. 3. Specifications of the camera used in photogrammetry study.

Table. 4. Soil parameters adopted in numerical analysis.

Table. 5. Maximum displacements at the pile capping beam along the selected locations and different epochs via cloud to cloud and cloud to mesh methods.

Table. 6. Maximum displacements at the pile capping beam at different epochs via all adopted methods.

Study	Method	Advantages	Disadvantages
Erol et al. [13]- Viaduct monitoring.	Global Positioning system (GPS) measurement	Provide high accuracy and simultaneous three-dimensional (3D) positioning	Costly
Xu et al. [14]- Preseismic deformation monitoring.		Greater flexibility in the selection of station locations	Time consuming
Luo et al. [15]- Freeze/thaw-induced deformation monitoring.		Can be carried out under different weather conditions	Low accuracy in determining real time movements
Gu et al. [36]- Crustal deformation monitoring.			Limited physical accessibility
Yang et al. [16]- Deformation monitoring.			Limited vertical displacement measurement
Kaloop et al. [31]- Beam deformation monitoring.	Total station surveying	Quick instrument setup	Low accuracy in determining real time movements
Lienhart [37]- Geotechnical monitoring.		Can be carried out under different weather conditions	Relatively costly
			Limited physical accessibility
			Digital elevation model (DEM) errors
			Accuracy depends on the target type
Massonnet et al. [32]- Earthquake displacement field mapping.	Interferometric synthetic aperture radar (InSAR) observation	Less costly than obtaining sparse point measurements from labor-intensive global positioning system (GPS) surveys	Low temporal sampling intervals
Rosen et al. [33]- Techniques of interferometry, systems and limitations, and applications.		Numerous data points	Single look direction
Yan et al. [34]- Subsidence measurement.			Limited vertical displacement measurement
Thakur et al. [38]- Snow cover area mapping.			
Sefa [35]- Land subsidence measurement.			

Hisham et al. [42]- Secant pile wall.	Fiber Optic Strain Sensing	Full length deflection profile	Local solution
		Can still be monitored long after the construction	Costly
		High accuracy	Affected by weather conditions
		Three-dimensional deformation (vertical and horizontal)	Limited physical accessibility
Xu et al. [43]- Large scale bored pile	Inclinometer	Full length deflection profile	Local solution
		Relatively low-cost	Accuracy is limited
			One-dimensional deformation (horizontal)
			Less stable results
			Limited physical accessibility
Wang et al. [8]- Landslide monitoring.	Terrestrial Laser Scanners (TLS)	Provides an effective and rapid solution to detect deformation on a large surface	Costly
Gui et al. [40]- Subway deformation monitoring.		Numerous data points	Affected by weather conditions
Xu et al. [39]- Composite structure deformation analysis.		Contact free with the scanned object	
		3 dimensional results	
Valença et al. [44]- Footbridge deformation monitoring.	Photogrammetry	Numerous data points	Accuracy is distance dependent
Han et al. [6]- Retaining wall displacement measurement.		Reduced time of field work	Accuracy is camera dependent
Scaioni et al. [7]- Tunnel monitoring.		3 dimensional results	Affected by weather conditions
Masoodi et al. [17]- Riverbank seepage erosion monitoring.		Cost effective	Limited physical accessibility
		Contact free with the scanned object	
Stalin et al. [41]- Mine modeling and mapping.	Photogrammetry with the aid of an Unmanned Air Vehicle (UAV)	Cost effective	Affected by weather conditions
Yutaka and Yoshihisa [18]- River topography monitoring.		Reduced time of field work	Accuracy is camera dependent

Congress and Puppala [19]- Transport infrastructure monitoring.		Accessibility to different locations	
Turner et al. [20]- Underground excavation mapping.		Can be automized	
		3 dimensional results	
		Contact free with the scanned object	
		Numerous data points	

Table. 1. Comparison of different deformation monitoring techniques.

Control Point	Y	X	Z
1	530188.444	3912026.156	45.799
2	530177.626	3912028.623	45.934
3	530174.532	3912017.127	46.221
4	530171.177	3912000.244	46.451
5	530172.505	3911992.085	46.703
6	530184.839	3911986.874	46.782

Table. 2. Control Point Coordinates taken by GNSS device.

Sensor	1/2.3” CMOS Effective pixels: 12.4 M (total pixels: 12.76 M)
Lens	FOV 94° 20 mm (35 mm format equivalent) f/2.8 focus at ∞
ISO Range	100-3200 (video) 100-1600 (photo)
Electronic Shutter Speed	8 - 1/8000 s
Image Size	4000×3000 pixels

Table. 3. Specifications of the camera used in photogrammetry study.

Mohr-Coulomb		1 Sandy-Clay	2 Silty-Clay	3 Stiff Clay	4 Marl
Type		Drained	Drained	UnDrained	UnDrained
γ_{unsat}	[kN/m³]	18.71	19.20	19.60	19.60
γ_{sat}	[kN/m³]	22.26	22.20	22.20	22.60
e_{init}	[-]	0.500	0.500	0.500	0.500
c_k	[-]	1E15	1E15	1E15	1E15
E_{ref}	[kN/m²]	5372.000	8690.000	14000.000	35708.000
ν	[-]	0.300	0.300	0.350	0.400
G_{ref}	[kN/m²]	2066.154	3342.308	5185.185	12752.857
E_{oed}	[kN/m²]	7231.538	11698.077	22469.136	76517.143
c_{ref}	[kN/m²]	83.00	21.00	135.38	288.00
φ	[°]	31.00	33.80	33.53	40.15

Table. 4. Soil parameters adopted in numerical analysis.

			LOCATION A		LOCATION B		LOCATION C	
Date of Monitoring	**Day(s)**	**Ref Depth (m)**	**cloud to cloud (mm)**	**cloud to mesh (mm)**	**cloud to cloud (mm)**	**cloud to mesh (mm)**	**cloud to cloud (mm)**	**cloud to mesh (mm)**
28.08.2017	0	0	0	0	0	0	0	0
06.09.2017	9	0	21	20	14	10	11	7
10.09.2017	13	0	23	24	23	24	12	9
17.09.2017	20	0	63	62	48	47	16	23
17.09.2017	20	-2					9	13
17.09.2017	20	-4					7	9

Table. 5. Maximum displacements at the pile capping beam along the selected locations and different epochs via cloud to cloud and cloud to mesh methods.

			LOCATION B		
Date of Monitoring	**Day(s)**	**Ref Depth (m)**	**Inclinometer (mm)**	**Cloud to Cloud (mm)**	**Strip (mm)**
28.08.2017	0	0	0	0	0
06.09.2017	9	0	15	14	17
10.09.2017	13	0	-	23	28
17.09.2017	20	0	52	48	57

Table. 6. Maximum displacements at the pile capping beam at different epochs via all adopted methods.

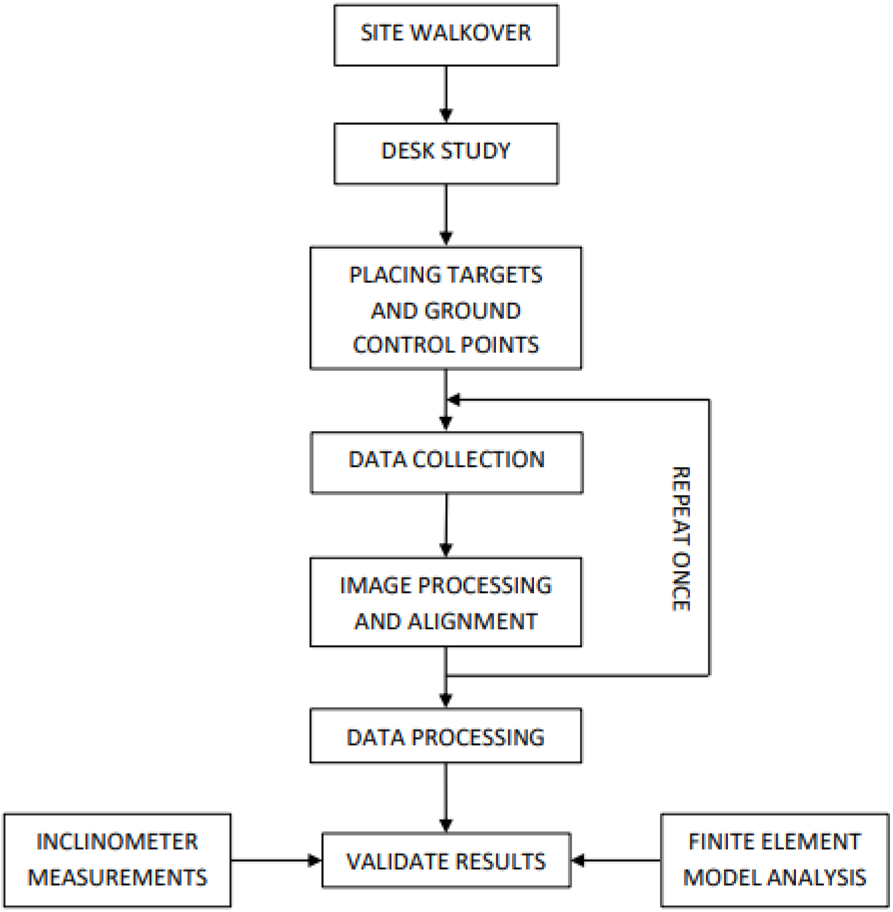

Figure 1 - Flowchart representing the steps followed in aerial close-range photogrammetry study.

Figure 2 - . Case study area aerial photographs and ground control points.

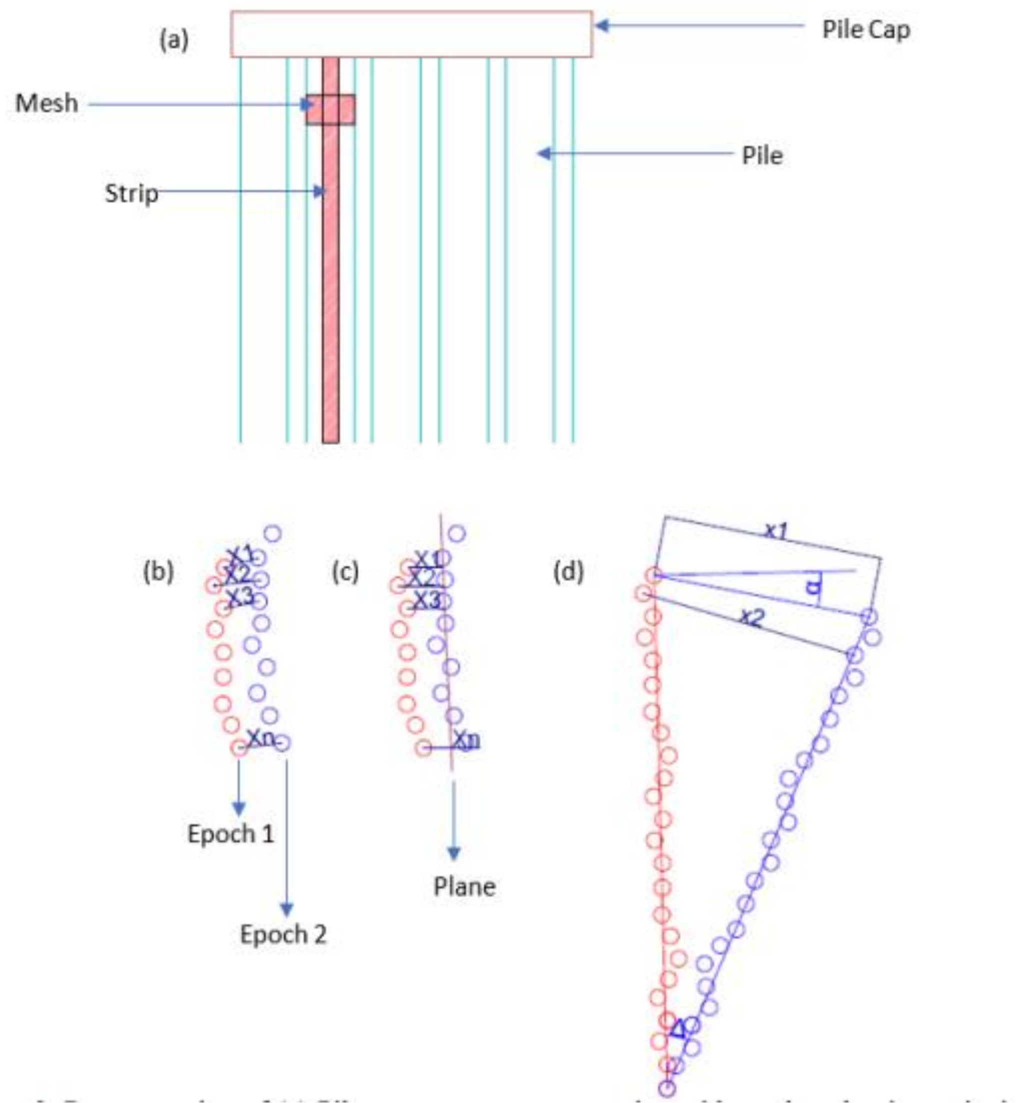

Figure 3 - . Representation of (a) Pile arrangement cross section with mesh and strip sectioning (b) Cloud to cloud (c) Cloud to mesh and (d) Strip

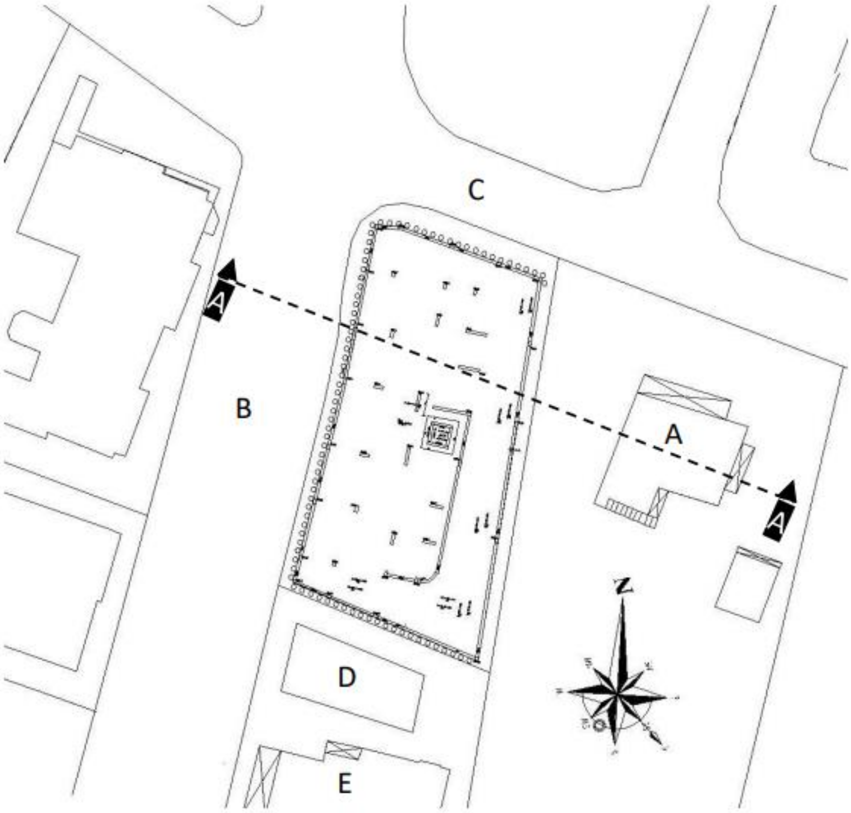

Figure 4 - . Layout of the case study area.

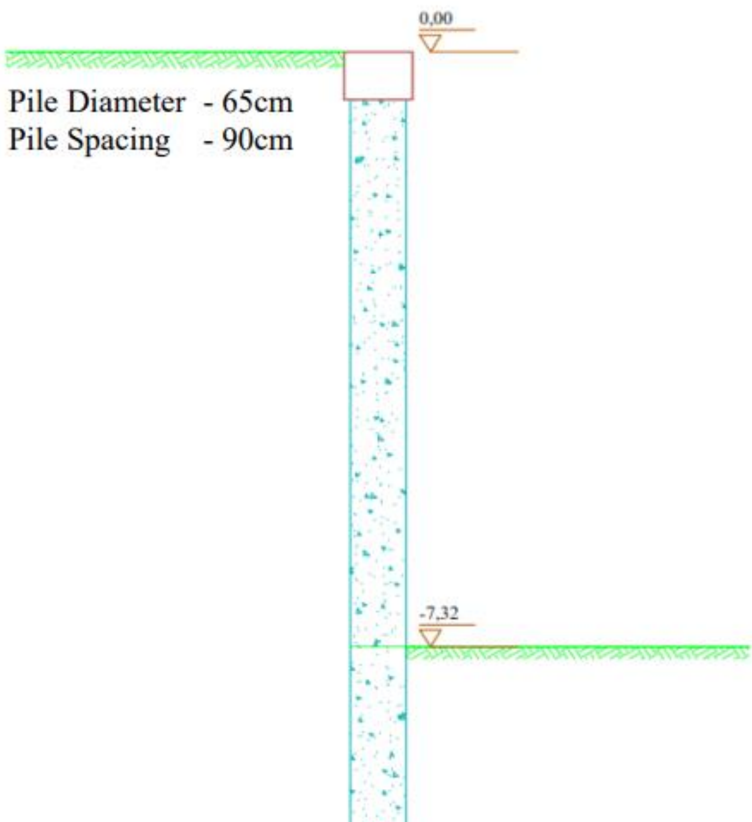

Figure 5 - Proposed cantilever retaining wall

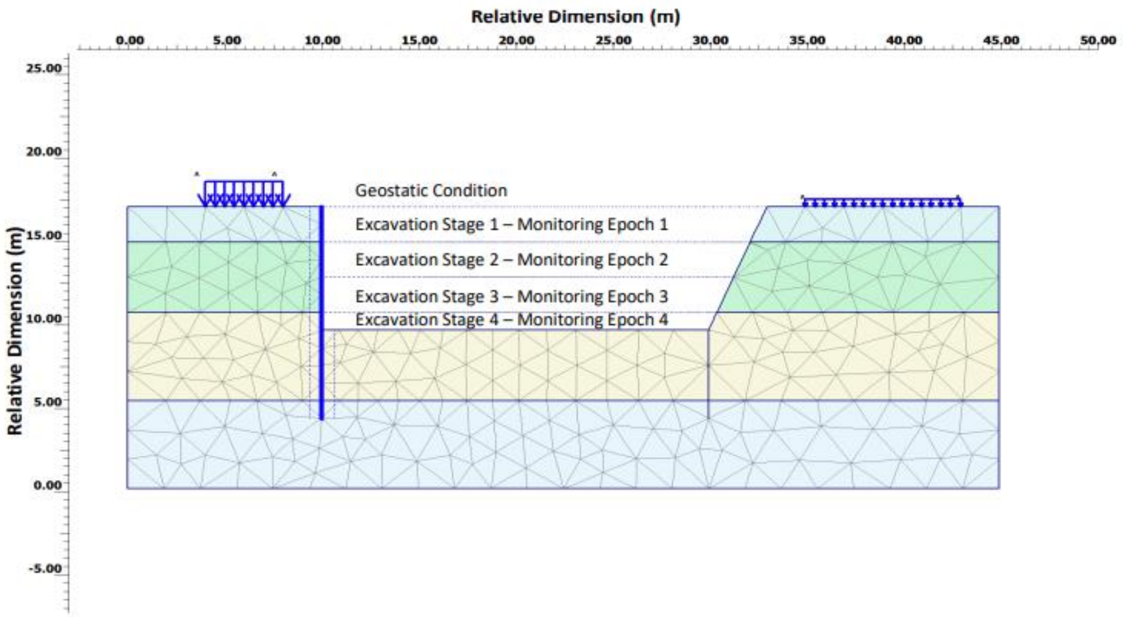

Figure 6 - Numerical analysis showing stages of excavation, monitoring and analysis.

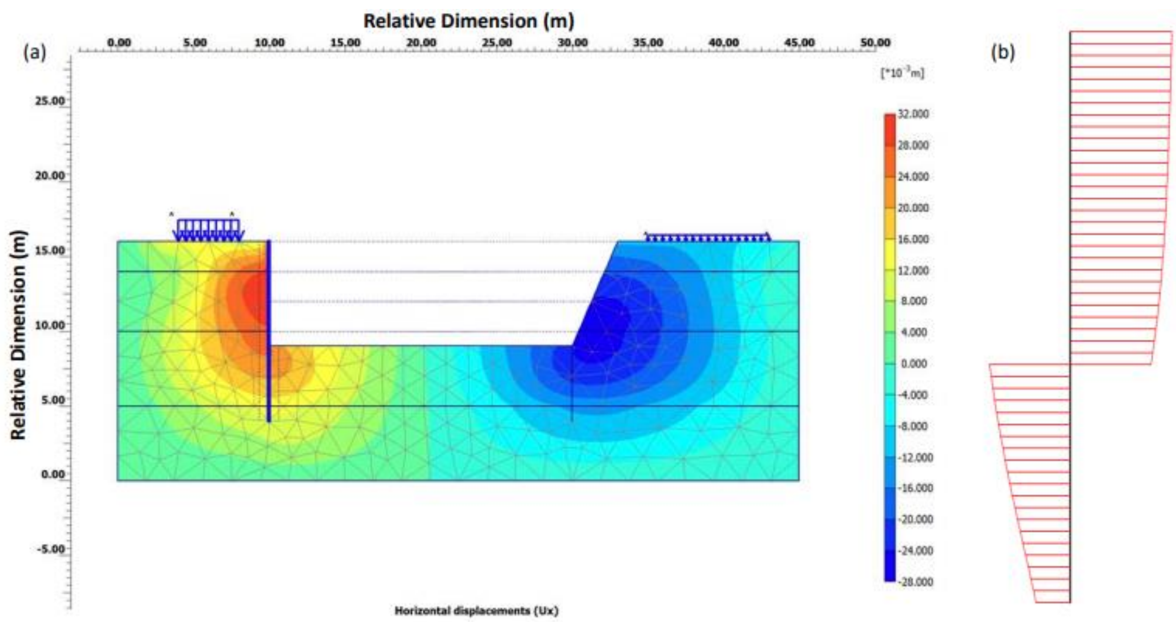

Figure 7 - Numerical analysis results (a) deformations along analyzed area and (b) variations of horizontal deformation along pile surface.

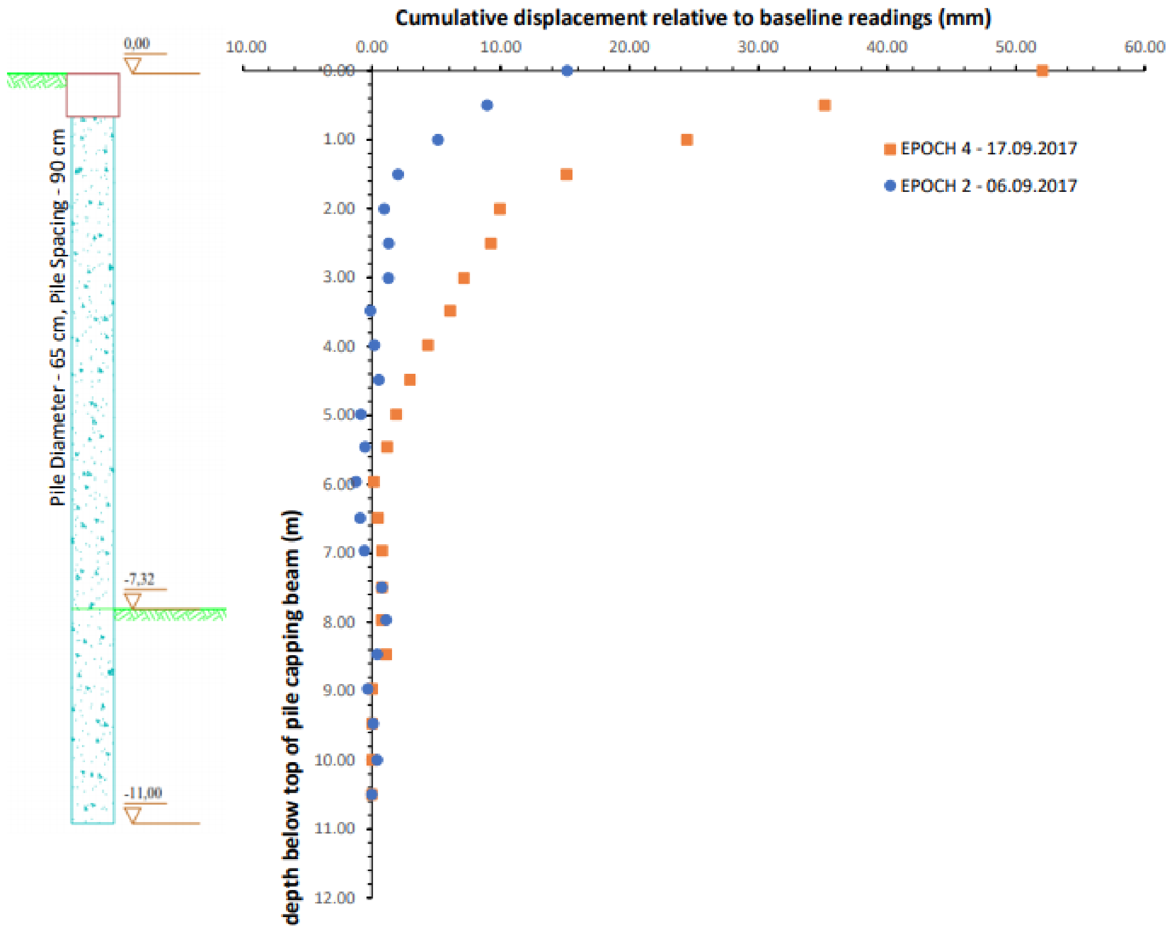

Figure 8 – Sketch of constructed cantilever retaining wall with inclinometer monitoring results.

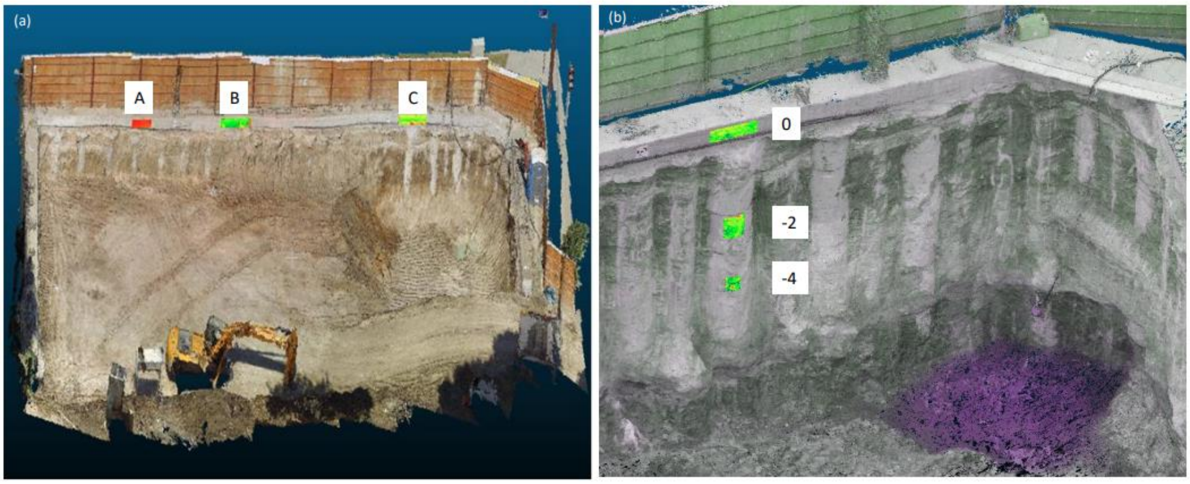

Figure 9 - Point Cloud of the excavation area with the location of the sections used for comparison.

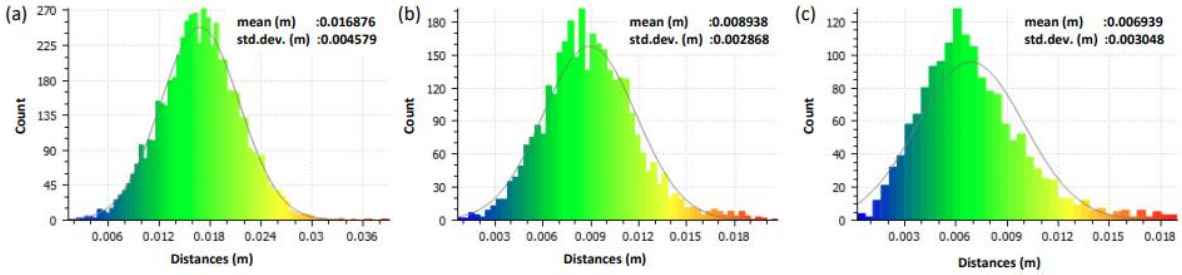

Figure 10 - Gauss distribution of Cloud to Cloud distance comparison at Location C at (a) 0m, (b) -2m, (c) -4m depth from reference point.

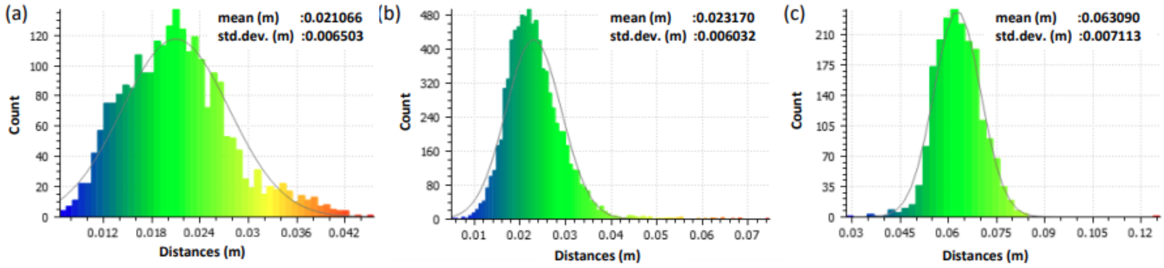

Figure 11 - Gauss distribution of Cloud to Cloud distance comparison at Location A (a) Epoch 1-2, (b) Epoch 1-3, (c) Epoch 1-4.

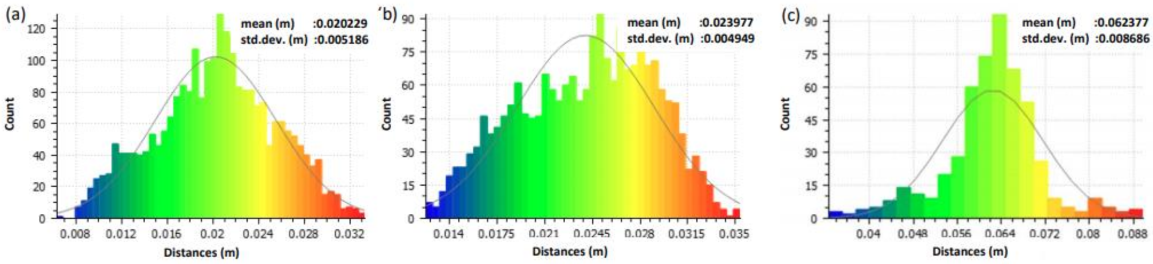

Figure. 12. Gauss distribution of Cloud to Mesh distance comparison at location A (a) Epoch 1-2, (b) Epoch 1-3, (c) Epoch 1-4.

Figure 12- Gauss distribution of Cloud to Mesh distance comparison at location A (a) Epoch 1-2, (b) Epoch 1-3, (c) Epoch 1-4.

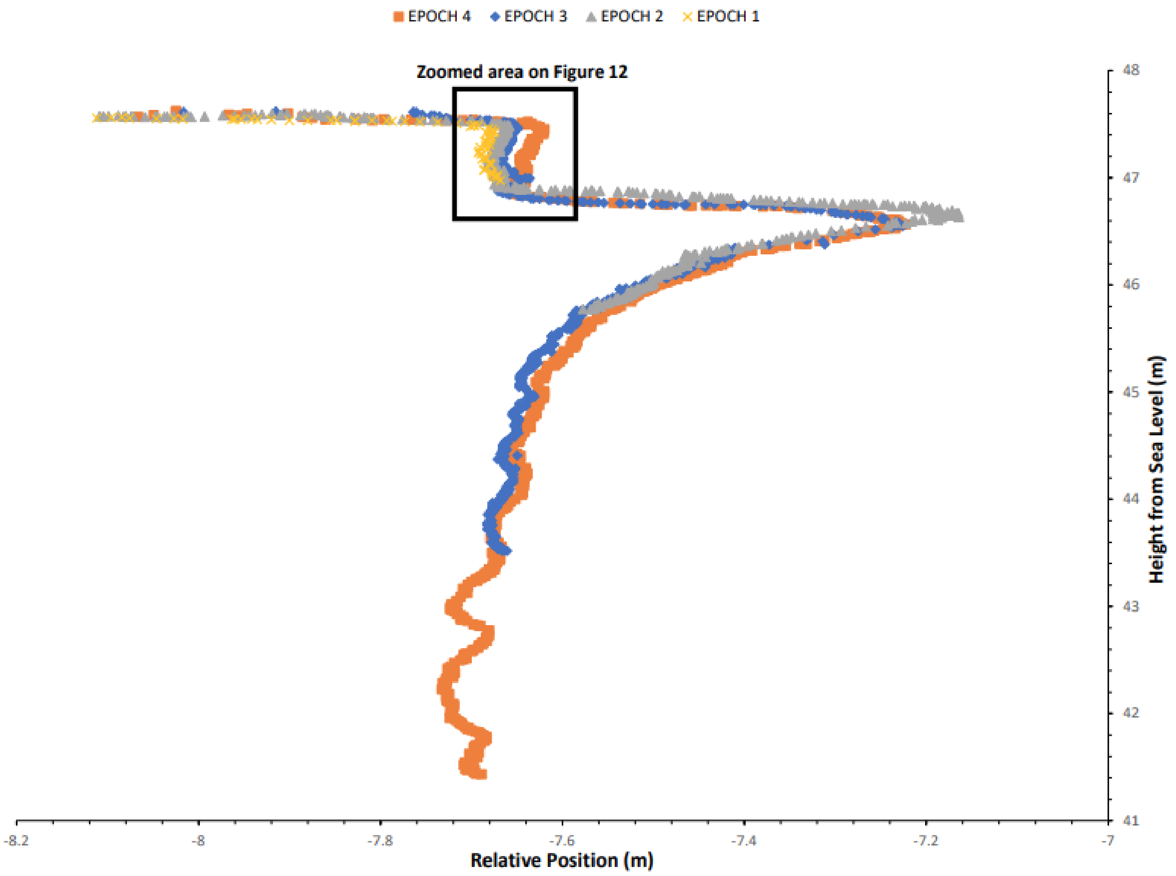

Figure 13 - . Comparison of epochs at location B with strip method.

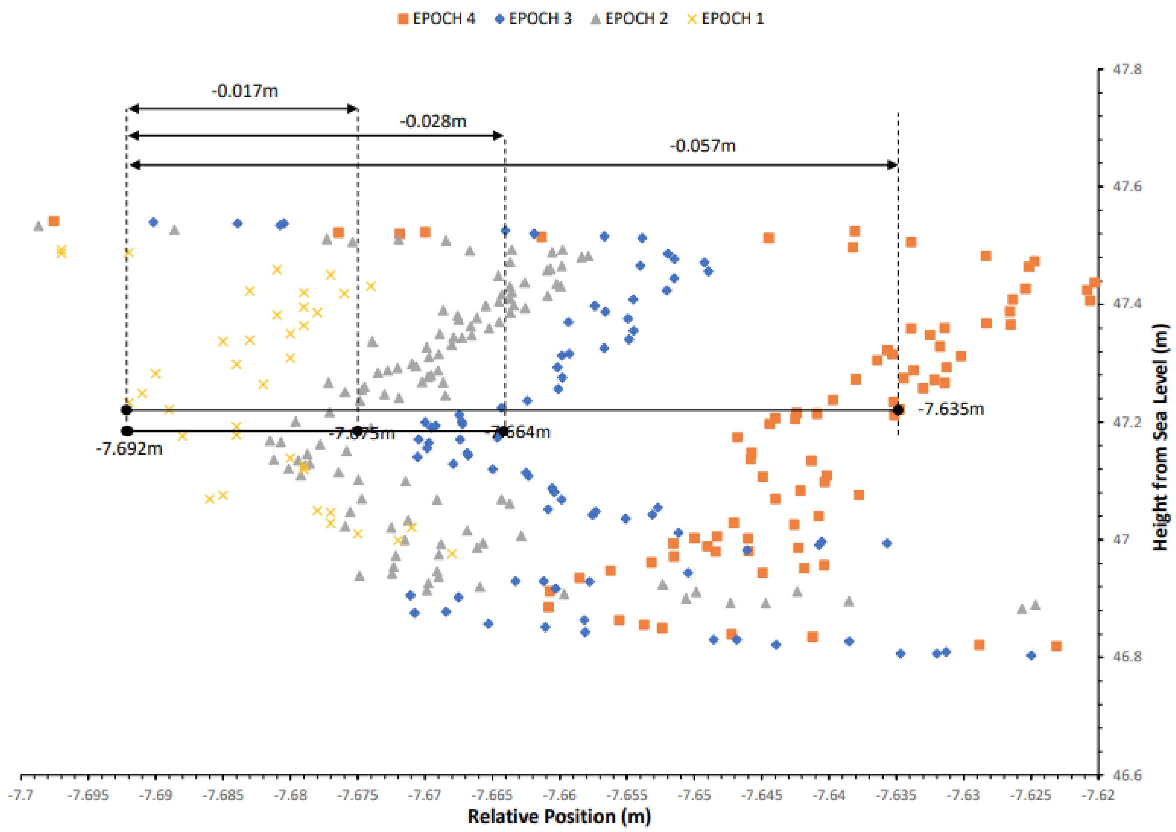

Figure 14 - Deflections of the pile at location B from height 46.6m above sea level to 47.8m above sea level.

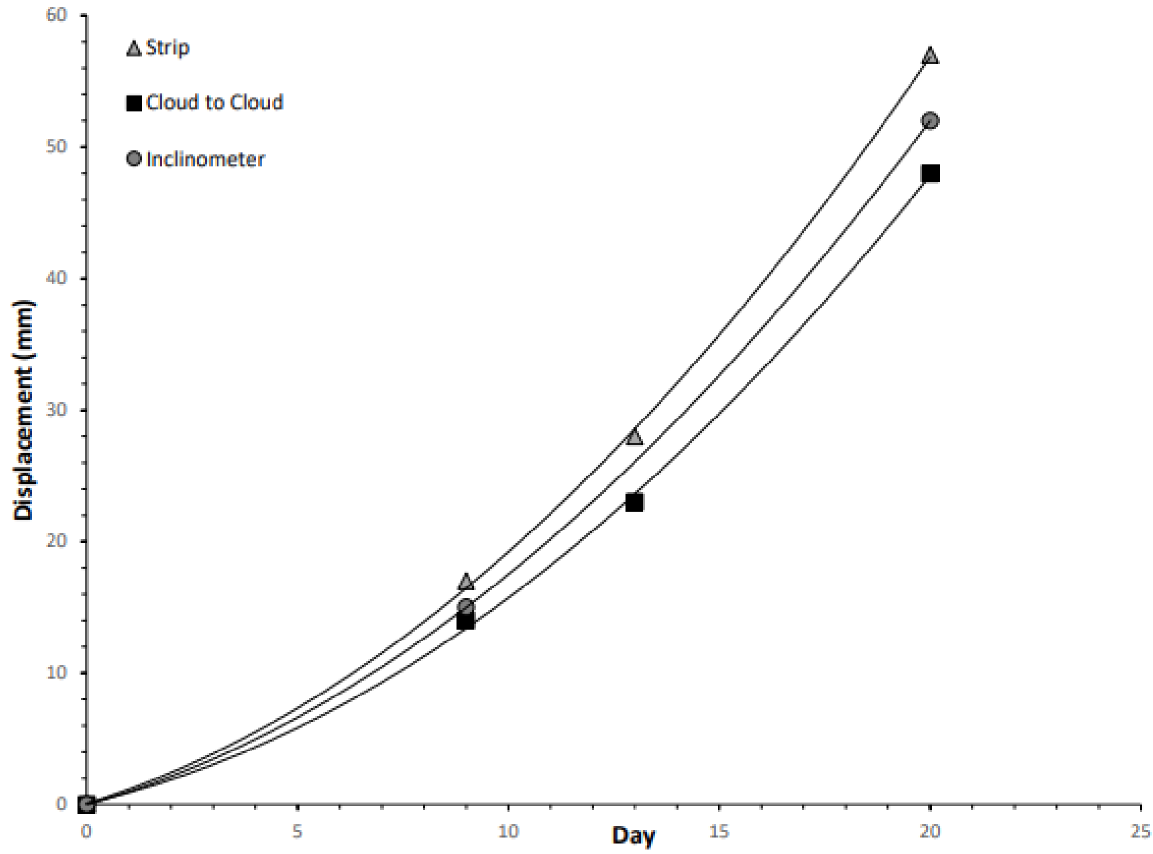

Figure 15 - Displacement of the pile capping beam at different epochs via Strip, Cloud to Cloud and Inclinometer measurements at location B.